High spin states of the normally deformed bands of ^{83}Y

W. Rodriguez,[1,*] F. Cristancho,[1] S. L. Tabor,[2] A. Kardan,[3] I. Ragnarsson,[4] R. A. Haring-Kaye,[5] J. Döring,[6,7] D. G. Sarantites,[8] and A. Garzón[9]

[1]*Universidad Nacional de Colombia, Sede Bogotá, Facultad de Ciencias, Departamento de Física, Bogotá 111321, Colombia*
[2]*Department of Physics, Florida State University, Tallahassee, Florida 32306, USA*
[3]*School of Physics, Damghan University, P.O. Box 36716-41167, Damghan, Iran*
[4]*Division of Mathematical Physics, LTH, Lund University, P.O. Box 118, SE-221 00 Lund, Sweden*
[5]*Department of Physics and Astronomy, Ohio Wesleyan University, Delaware, Ohio 43015, USA*
[6]*Department of Physics, University of Notre Dame, Notre Dame, Indiana 46556, USA*
[7]*Bundesamt für Strahlenschutz, D-10318 Berlin, Germany*
[8]*Chemistry Department, Washington University, St. Louis, Missouri 63130, USA*
[9]*Departamento de Matemáticas, Universidad Sergio Arboleda, Bogotá, Colombia*

(Received 5 June 2019; published 19 August 2019)

Level lifetime and side-feeding time measurements were performed on the excited states of the normally deformed bands of ^{83}Y using the Doppler-shift attenuation method (DSAM). The high spin states of ^{83}Y were populated using the fusion-evaporation reaction ^{58}Ni(^{32}S, $\alpha 3p$)^{83}Y at 135 MeV. Twenty-two level lifetime and side-feeding times were determined in most of the cases by comparing the line shapes gated with transitions above and below the state under study. Quadrupole moments determined from lifetime measurements are in the range 1.1–3.1 eb, and are similar to the ones found for some of the neighboring nuclei. The measured side-feeding times were compared with predictions made by simulations carried out with the GAMMAPACE code. The results were in agreement with the experimental values by assuming reduced transition probabilities of the collective transitions in the continuum region, lying in the range 40–80 W.u. The discrete excited states were studied with paired cranked Nilsson-Strutinsky-Bogoliubov (CNSB) calculations carried out for the first time for an $A \approx 80$ nucleus. Unpaired cranked Nilsson-Strutinsky (CNS) calculations were used to specify configurations and study the band crossings. The measured $|Q_t|$ values show a general agreement with CNSB calculations. Cranked shell model analysis evinced that the smallest quadrupole moment appears at the sharpest band crossing of the bands studied and CNSB calculations show an increase of the deformation thereinafter.

DOI: 10.1103/PhysRevC.100.024327

I. INTRODUCTION

Neutron deficient nuclei with $A \approx 80$ lie in the region where numbers of both neutrons and protons are in the middle between the magic numbers 28 and 50. Discrete excited states of these nuclei have shown rotational behavior (see for example [1]). Several phenomena like shape evolution, band termination, and band crossings and their relation with the behavior of quasiparticle energies and alignment have been studied in nuclei in this region. In particular, from ^{83}Y excited states band termination remains to be studied, and a deeper study can be carried out for the other phenomena along with interpretations under new theoretical models.

Lifetime measurements of collective excited states provide the most powerful tool to determine quadrupole moments of deformed nuclei. Nevertheless some experimental difficulties arise when measuring the lifetimes of high spin states. One of them is the fact that the required intensity for such measurements should be much higher than the one required to build the level scheme. Another experimental difficulty is the wide time range, in cases as wide as four orders of magnitude, typically found for lifetimes of states going from high to low spin sates. This lifetime range makes it difficult, or in most of the cases not possible, to optimize a single experiment for the measurement of the lifetimes of all of the interesting states. Therefore several experiments are required to study a single nucleus. For the ^{83}Y case, the nuclear structure of the first excited states of the yrast band was previously studied by lifetime measurements using different methods [2–4]. The recoil distance Doppler shift attenuation method (RDSAM) was implemented with the reaction ^{54}Fe(^{32}S, $3p$)^{83}Y at 105 MeV to measure lifetimes of low spin states [3]. The most complete version of the level scheme of ^{83}Y is reported in Ref. [5], where lifetimes of some excited states were also published. Nonetheless the lifetimes of most of the states currently known for ^{83}Y have not been measured, which has prevented a complete study of the nuclear shape evolution of this nucleus. Moreover, the methodology used in Refs. [2–5] involves the simultaneous measurement of side-feeding times and level lifetimes, i.e., using the same line shape, possibly introducing nonvalid correlations between these lifetimes. In the present

*wrodriguezh@unal.edu.co

work that problem is avoided by obtaining line shapes using both gates from above (GFA) and gates from below (GFB) the transition of interest, where possible.

It was mentioned in Ref. [5] that one of the negative parity bands was observed very likely reaching terminating state. However, no quadrupole moments were available to support the explanation of the band termination phenomenon. The results presented here aim to complement the current information on nuclear structure of normally deformed bands of ^{83}Y by means of lifetime measurements using GFA and GFB. These measurements will provide more precise determination of quadrupole moments, providing better and new data to be compared with the theoretical models.

II. EXPERIMENT AND DATA ANALYSIS

High spin states of ^{83}Y were populated through the reaction $^{32}\mathrm{S} + {}^{58}\mathrm{Ni}$ at 135 MeV conducted at Lawrence Berkeley National Laboratory. A 415 μg/cm^2 ^{58}Ni target followed by a backing of 10.3 mg/cm^2 of ^{181}Ta were used in an experiment optimized for Doppler shift attenuation (DSA) measurements. Fusion evaporation products were identified by detecting the emitted charged particles with the Microball array [6], which consists of 95 CsI(Tl) detectors set up in a 4π arrangement covering 97% of 4π. γ rays were detected by the Gammasphere array [7], which consists of 110 high-purity germanium (HPGe) detectors surrounded by bismuth germanate (BGO) Compton suppressor detectors arranged in a spherical configuration. The Gammasphere detectors are arranged in 17 rings, each one located at a different polar angle with its detectors uniformly distributed over the azimuthal angle. Two consecutive pairs of rings were used in combination for the DSA line-shape measurements. For each pair of rings the weighted average angle was used. Therefore line shapes measured at $\bar{\theta} = 35.0^\circ, 145.5^\circ, 52.8^\circ, 127.2^\circ$ were used in the lifetime analysis. For the selection of ^{83}Y events, the detection of one α particle and three protons in Microball was set as a condition for selecting the γ -rays to analyze. The selected data were sorted out in γ-γ matrices containing in the y axis the γ rays detected at any angle and in the x axis the γ rays detected at the $\bar{\theta}$ angles. Doppler correction over the y axis was applied with β/c values ranging from 0.00 to 0.04 in order to perform the gates to study the line shapes observed at different angles.

Figure 1 shows a partial level scheme of normally deformed bands of ^{83}Y singling out relevant states and transitions for this work, determined from the transitions observed in the data analyzed here and complemented with transitions reported in Ref. [5]. Interband transitions shown in previous publications [5,8] were not observed in this analysis, probably because of low intensity, making them not relevant for the lifetime measurements presented here. For this reason such transitions were omitted in Fig. 1. The transitions from states at $(39/2^-)$, $(47/2^+)$, $(51/2^+)$, and $(53/2^+)$ were not observed in our data. They are included in Fig. 1 for completeness, as spin and parities; they were taken from Ref. [5]. The labels of the bands were assigned using parity π and signature α as (π, α) and the equivalences $\alpha = +1/2 \equiv +$ and $\alpha = -1/2 \equiv -$ were used. This labeling coincides with the one adopted in Ref. [8].

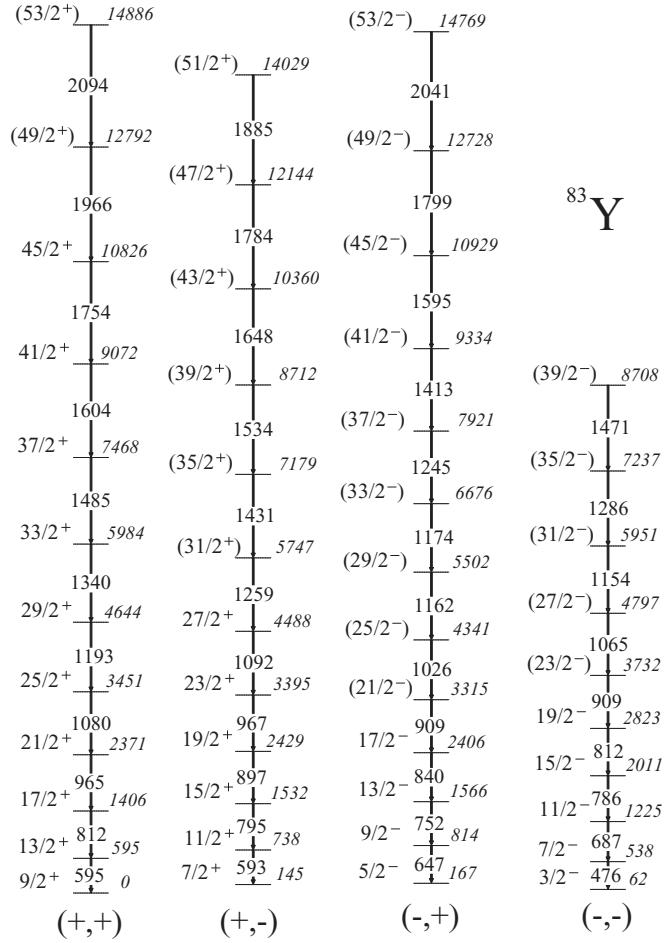

FIG. 1. Partial level scheme of ^{83}Y showing normally deformed bands as determined from the data analyzed in this work and complemented with transitions observed in Ref. [5] at $(47/2^+)$, $(51/2^+)$, $(53/2^+)$, and $(39/2^-)$.

A. Lifetime measurements

The stopping time of the ^{83}Y nucleus inside the ^{181}Ta backing is around 1 ps; a value that becomes the upper limit for the lifetimes that can be obtained with the data acquired in this experiment. For states having lifetimes around 1 ps or larger, the line shape obtained for its depopulating transition does not show a Doppler broadening, which prevents the lifetime determination by DSAM. Thus lifetimes were determined starting from the highest spin state populated down to the states at $21/2^+$, $19/2^+$, and $(25/2^-)$ for the $(+, +)$, $(+, -)$, and $(-, +)$ bands respectively.

Figure 2 shows the line shapes measured for some of the transitions in the $(+, -)$ band when gating at $E_\gamma = 897$ keV. The sensitivity of the line shape of different transitions produced by states having different feeding population and lifetimes can be visualized.

Some of the lifetimes reported in this work were previously evaluated using the same dataset analyzed in this work by

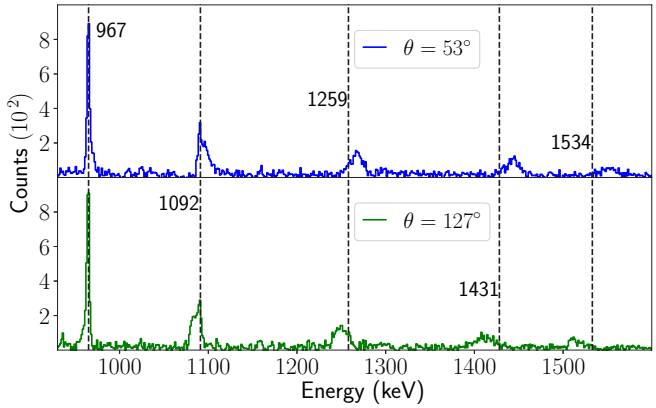

FIG. 2. Spectra showing transitions of the $(+,-)$ band detected at $\bar{\theta} = 52.8°, 127.2°$. The spectra were obtained by a GFB on the transition of 897 keV. The vertical dashed lines indicate the transition energies.

using gates from below only, except for one of the transitions [9]. In this work it was possible to obtain line shapes by gating from above for most of the states studied here, including high spin states. Figure 3 shows the measured and calculated line shapes of the 1799 keV, $49/2^- \rightarrow 45/2^-$ transition in the $(-,+)$ band when gating from above at the 2041 keV transition. By taking the average of the lifetimes measured for the four θ angles, as shown in Fig. 3, the precision of measurement is increased.

The determination of the level lifetimes τ and side-feeding times τ_{SF} was carried out by comparison of the experimental line shapes with the simulated ones produced by the AHKIN code [10]. This program simulates the slowing down of ^{83}Y nuclei as they travel through the ^{181}Ta stopper using the one-dimensional stopping power (generated by the program SRIM [11]) and the Blaugrund approximation for velocity straggling. The finite angular aperture of the Gammasphere detectors is considered when computing the probability distribution of the γ rays hitting the detectors at different angles. By

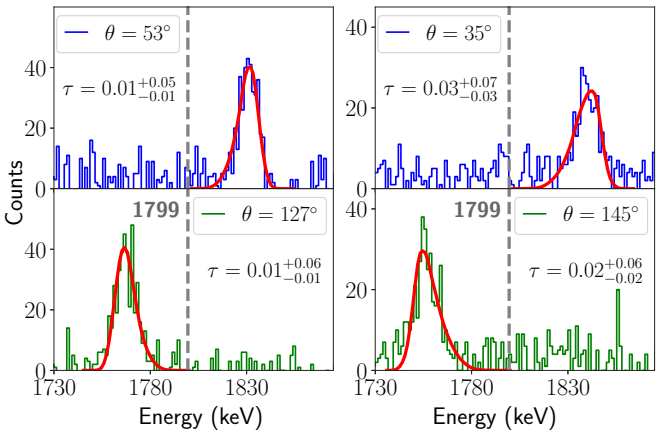

FIG. 3. 1799 keV $49/2^- \rightarrow 45/2^-$ transition line shape in the $(-,+)$ band gated from above at 2041 keV. The four angles used in the analysis are shown together with the lifetime found for each angle.

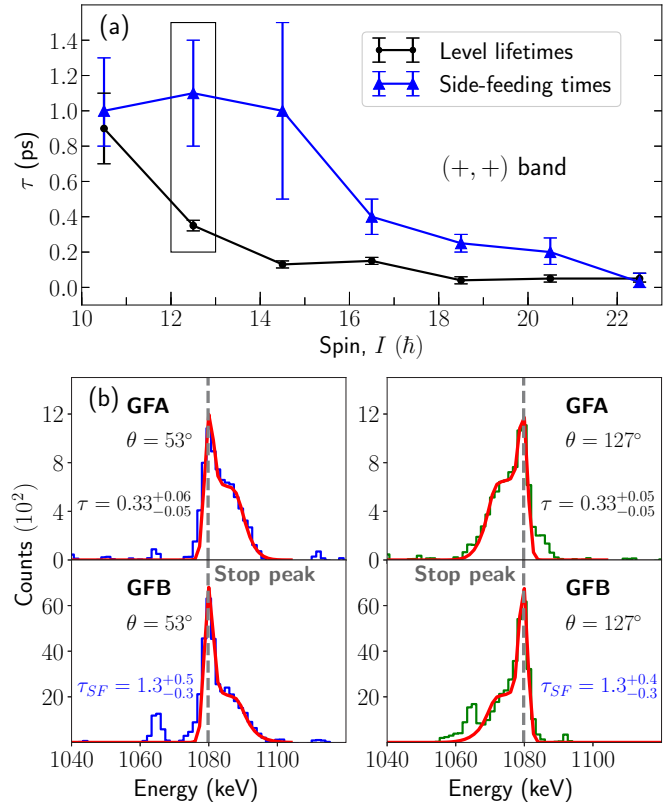

FIG. 4. (a) Level lifetime and side-feeding times for the $(+,+)$ band. It can be seen that in general $\tau_{SF} \gtrsim \tau$. The rectangle encloses the state of $I^\pi = 25/2^+$ emitting the γ ray of 1080 keV. (b) Line shape of the 1080 keV transition compared when applying GFA at 1340 keV and GFB at 595 keV for $\theta = 53°$ and $\theta = 127°$.

solving the differential decay equations involving the initial feeding states and their initial relative population, AHKIN provides a line shape depending on the lifetime of the state under study for each detection angle. Minimization of the reduced value of chi squared (χ^2_r), used to compare the line shapes produced by AHKIN for different values of τ with the experimental spectrum, yields the measured lifetime and its uncertainty.

By performing GFA and GFB, side-feeding times can also be extracted. Figure 4(b) shows the line shapes of the 1080 keV transition when applying gates from above and from below. It can be seen that the relative number of counts in the "stop peak" increases in the GFB line shape compared with the GFA line shape, indicating a larger value of τ_{SF} compared with τ. In general the measured values follow the inequality $\tau_{SF} \gtrsim \tau$, as can be seen in Fig. 4(a) for the $(+,+)$ band.

In some cases GFA line shapes could not be obtained because of interference with other transitions. For instance in the $(-,+)$ band the 1174 and 1161 keV transitions are very close in energy to each other. When doing GFA for analysis of the 1174 keV transition, the line shape overlaps with the 1161 keV line shape. By applying GFB at the 1161 keV transition the interference with 1174 keV can be removed. For these special cases the determination of τ and τ_{SF} was done by applying a correlation method. In that method a minimization

TABLE I. Level energies E_x, spins and parities I^π, transition γ-ray energies E_γ, and τ and τ_{SF} for the $(+,+)$, $(+,-)$ and $(-,+)$ bands of ^{83}Y.

E_x (keV)	I^π ($\hbar$)	E_γ (keV)	τ (ps)[a]	τ (ps)[b]	τ (ps)	τ_{SF} (ps)
			$(+,+)$ band			
12792	$(49/2^+)$	1966		$0.01^{+0.05}_{-0.01}$	$0.10^{+0.03}_{-0.02}$ [c]	
10826	$45/2^+$	1754		$0.02^{+0.08}_{-0.01}$	$0.05^{+0.03}_{-0.02}$	$0.03^{+0.05}_{-0.03}$
9072	$41/2^+$	1604		$0.02^{+0.08}_{-0.01}$	$0.05^{+0.02}_{-0.02}$	$0.20^{+0.08}_{-0.07}$
7468	$37/2^+$	1485		$0.07^{+0.04}_{-0.03}$	$0.04^{+0.02}_{-0.02}$	$0.25^{+0.05}_{-0.05}$
5984	$33/2^+$	1340	$\leqslant$0.39	$0.32^{+0.13}_{-0.10}$	$0.15^{+0.02}_{-0.02}$	$0.4^{+0.1}_{-0.1}$
4644	$29/2^+$	1193	0.29(7)	$0.28^{+0.05}_{-0.04}$	$0.13^{+0.02}_{-0.02}$	$1.0^{+0.5}_{-0.5}$
3451	$25/2^+$	1080	0.38(8)		$0.35^{+0.03}_{-0.03}$	$1.1^{+0.3}_{-0.3}$
2371	$21/2^+$	965	0.6(1)		$0.9^{+0.2}_{-0.2}$	$1.0^{+0.3}_{-0.2}$
1406	$17/2^+$	812	1.39(15)			
595	$13/2^+$	595	7.8(7)			
			$(+,-)$ band			
10360	$(43/2^+)$	1648			$0.16^{+0.11}_{-0.07}$ [c]	
8712	$(39/2^+)$	1534			$0.04^{+0.02}_{-0.02}$	$0.2^{+0.4}_{-0.1}$
7179	$(35/2^+)$	1431		<0.34	$0.07^{+0.03}_{-0.02}$	$0.4^{+0.2}_{-0.2}$
5747	$(31/2^+)$	1259		$0.29^{+0.11}_{-0.10}$	$0.20^{+0.06}_{-0.06}$	$0.6^{+1.2}_{-0.5}$
4488	$27/2^+$	1092		$0.29^{+0.09}_{-0.11}$	$0.35^{+0.11}_{-0.07}$ [d]	$0.2^{+1.1}_{-0.2}$ [d]
3395	$23/2^+$	967		$0.62^{+0.16}_{-0.13}$	$0.6^{+0.2}_{-0.1}$ [d]	$0.3^{+1.0}_{-0.2}$ [d]
			$(-,+)$ band			
14769	$(53/2^-)$	2041			$0.08^{+0.04}_{-0.03}$ [c]	
12728	$(49/2^-)$	1799			$0.01^{+0.03}_{-0.01}$	$0.02^{+0.05}_{-0.02}$
10929	$(45/2^-)$	1595			$0.03^{+0.04}_{-0.02}$	$0.09^{+0.17}_{-0.07}$
9334	$(41/2^-)$	1413			$0.10^{+0.03}_{-0.03}$ [d]	$0.01^{+0.22}_{-0.01}$ [d]
7921	$(37/2^-)$	1245			$0.24^{+0.10}_{-0.09}$ [d]	$0.07^{+0.79}_{-0.07}$ [d]
6676	$(33/2^-)$	1174			$0.78^{+0.14}_{-0.11}$ [d]	$0.7^{+0.5}_{-0.3}$ [d]
5502	$(29/2^-)$	1162			$0.16^{+0.09}_{-0.06}$	$0.9^{+0.3}_{-0.2}$
4341	$(25/2^-)$	1026			$0.22^{+0.13}_{-0.11}$	$0.7^{+0.8}_{-0.2}$

[a]Values adopted in Ref. [3].
[b]Values reported in Ref. [5].
[c]Effective lifetime, not corrected by feeding.
[d]Lifetime determined by gating from below only.

of the χ^2_r for each of the variables τ and τ_{SF} is carried out using the same line shape obtained with the GFB only.

Regarding the $(-,-)$ band, some of the transitions shown in Fig. 1 were observed, although with very low intensity. Lifetime measurements were not possible for any of these states. For the 909 keV γ ray, emitted by the $(23/2^-)$ state, no Doppler broadening was observed, showing that its lifetime is around 1 ps or above. For the 1065, 1154, and 1286 keV γ rays the low intensity did not allow the line-shape analysis.

Table I shows the measured τ and τ_{SF} in this work alongside previously reported values.

The following section will present reduced transition probabilities $B(E2)$, transition quadrupole moments Q_t, and quadrupole deformation parameters β_2 determined from the measured lifetimes.

III. RESULTS

A. Level lifetimes

$B(E2)$ can be determined by means of the relation [12]

$$B(E2)(\text{W.u.}) = \frac{815.6 \times b}{[E_\gamma(\text{MeV})]^5\, \tau(\text{ps}) \times 0.0594 \times A^{4/3}}, \quad (1)$$

where the term $0.05940 \times A^{4/3}$ corresponds to one Weisskopf unit (W.u.) and b is the branching ratio. Table II shows the $B(E2)$ values that were determined from the measured τ and E_γ. These values vary around 80 W.u., demonstrating a large degree of collectivity in the transitions analyzed, which is in agreement with the rotational behavior observed for these states.

TABLE II. Level energies E_x, spins and parities I^π, transition energies E_γ, reduced transition probabilities $B(E2)$, transition electric quadrupole moments $|Q_t|$, and quadrupole deformation β_2 (assuming $\gamma = 0^\circ$ or $\gamma = -60^\circ$) for three normally deformed bands of ^{83}Y.

E_x (keV)	I^π ($\hbar$)	E_γ (keV)	$B(E2)$ (W.u.)	$\lvert Q_t\rvert$ (eb)	$\lvert\beta_2\rvert$[a]
			(+, +) band		
12792	$(49/2^+)$	1966	13^{+3}_{-3} [b]	$0.9^{+0.1}_{-0.1}$ [b]	$0.08^{+0.01}_{-0.01}$ [b]
10826	$45/2^+$	1754	50^{+30}_{-20}	$1.7^{+0.5}_{-0.4}$	$0.15^{+0.05}_{-0.04}$
9072	$41/2^+$	1604	70^{+50}_{-20}	$2.2^{+0.6}_{-0.3}$	$0.19^{+0.07}_{-0.03}$
7468	$37/2^+$	1485	130^{+130}_{-40}	$3.0^{+0.1}_{-0.6}$	$0.27^{+0.13}_{-0.06}$
5984	$33/2^+$	1340	59^{+9}_{-7}	$2.1^{+0.2}_{-0.1}$	$0.21^{+0.02}_{-0.01}$
4644	$29/2^+$	1193	120^{+20}_{-20}	$3.1^{+0.3}_{-0.2}$	$0.31^{+0.03}_{-0.02}$
3451	$25/2^+$	1080	74^{+7}_{-6}	$2.5^{+0.1}_{-0.1}$	$0.26^{+0.01}_{-0.01}$
2371	$21/2^+$	965	50^{+14}_{-9}	$2.3^{+0.3}_{-0.2}$	$0.23^{+0.02}_{-0.03}$
			(+, −) band		
10360	$(43/2^+)$	1648	20^{+15}_{-8} [b]	$1.1^{+0.4}_{-0.3}$ [b]	$0.11^{+0.04}_{-0.03}$ [b]
8712	$(39/2^+)$	1534	110^{+100}_{-40}	$2.7^{+1.1}_{-0.5}$	$0.28^{+0.11}_{-0.05}$
7179	$(35/2^+)$	1431	90^{+40}_{-30}	$2.5^{+0.5}_{-0.4}$	$0.25^{+0.05}_{-0.04}$
5747	$(31/2^+)$	1259	50^{+20}_{-10}	$1.9^{+0.4}_{-0.2}$	$0.20^{+0.04}_{-0.02}$
4488	$27/2^+$	1092	50^{+10}_{-10} [c]	$1.9^{+0.2}_{-0.2}$ [c]	$0.21^{+0.02}_{-0.02}$ [c]
3395	$23/2^+$	967	70^{+10}_{-20} [c]	$2.3^{+0.2}_{-0.3}$ [c]	$0.24^{+0.02}_{-0.03}$ [c]
			(−, +) band		
14769	$(53/2^-)$	2041	13^{+7}_{-4} [b]	$0.9^{+0.2}_{-0.1}$ [b]	$0.09^{+0.02}_{-0.01}$ [b]
12728	$(49/2^-)$	1799	140^{+4470}_{-100}	$2.9^{+14.0}_{-1.3}$	$0.30^{+1.41}_{-0.13}$
10929	$(45/2^-)$	1595	140^{+860}_{-90}	$2.9^{+4.9}_{-1.1}$	$0.30^{+0.49}_{-0.13}$
9334	$(41/2^-)$	1413	65^{+30}_{-20} [c]	$2.0^{+0.4}_{-0.3}$ [c]	$0.20^{+0.04}_{-0.03}$ [c]
7921	$(37/2^-)$	1245	50^{+30}_{-20} [c]	$1.8^{+0.5}_{-0.3}$ [c]	$0.18^{+0.05}_{-0.03}$ [c]
6676	$(33/2^-)$	1174	22^{+4}_{-3} [c]	$1.2^{+0.7}_{-0.5}$ [c]	$0.12^{+0.01}_{-0.01}$ [c]
5502	$(29/2^-)$	1162	120^{+80}_{-40}	$2.7^{+0.8}_{-0.5}$	$0.28^{+0.08}_{-0.06}$
4341	$(25/2^-)$	1026	150^{+150}_{-60}	$3.1^{+1.3}_{-0.6}$	$0.31^{+0.13}_{-0.07}$

[a]Values calculated with an approximated formula assuming axial symmetry in order to provide a general idea on how large the deformation is.
[b]Values calculated using the effective lifetime and thus only providing a lower limit of the value.
[c]Lifetime was determined by gating from below only.

Q_t can be calculated by means of the relation in Ref. [12],

$$|Q_t| = \sqrt{\frac{16\pi}{5}}\frac{\sqrt{B(E2)}}{|\langle I, K; 20|I-2, K)|}, \tag{2}$$

where K is the component of the nuclear spin along the rotation axis and I is the spin of the initial state of the transition. Following Eqs. (1) and (2) the $|Q_t|$ values were calculated and the results are shown in Table II.

The quadrupole deformation β_2 and the transition quadrupole moment Q_t can be related. Starting from the relation in Ref. [13] for Q_{20} and multiplying it by $\cos(30^\circ + \gamma)/\cos(30^\circ)$ [14], the relation (3) is obtained:

$$Q_t = \frac{6ZeA^{2/3}}{(15\pi)^{1/2}} r_0^2 \beta_2 (1 + 0.16\beta_2)\cos(30^\circ + \gamma). \tag{3}$$

For $\beta_2 \approx 0.3$, the term $0.16\beta_2$ takes values $\approx$0.05, which implies a contribution to Q_t smaller than the values of the experimental uncertainties. Therefore Eq. (3) can be simplified for this case as

$$|Q_t| = \frac{6ZeA^{2/3}}{(15\pi)^{1/2}} r_0^2 |\beta_2| \cos(30^\circ + \gamma), \tag{4}$$

where it was also taken into account that only the absolute value of β_2 can be calculated since from the experimental values we can only determine the absolute value of the quadrupole moments. In Eqs. (3) and (4) $\gamma = 0^\circ$ and $\gamma = -60^\circ$ represent the maximum collectivity values for a prolate shape ($\gamma = 0^\circ$) and an oblate shape ($\gamma = -60^\circ$). As reference values to calculate $|\beta_2|$ we take $\gamma = 0^\circ$ or $\gamma = -60^\circ$, both producing the same results in Eq. (4). The values of $|\beta_2|$ found are reported in Table II, where it can be seen that $0.18 \lesssim |\beta_2| \lesssim 0.31$, which corresponds to normally deformed band values.

The $|Q_t|$ values determined in this work are shown in Fig. 5 together with the previously reported values. For the (+, +) band, the values for the $I \geqslant 37/2$ states are in agreement with the values reported in Ref. [5]. The previously reported values

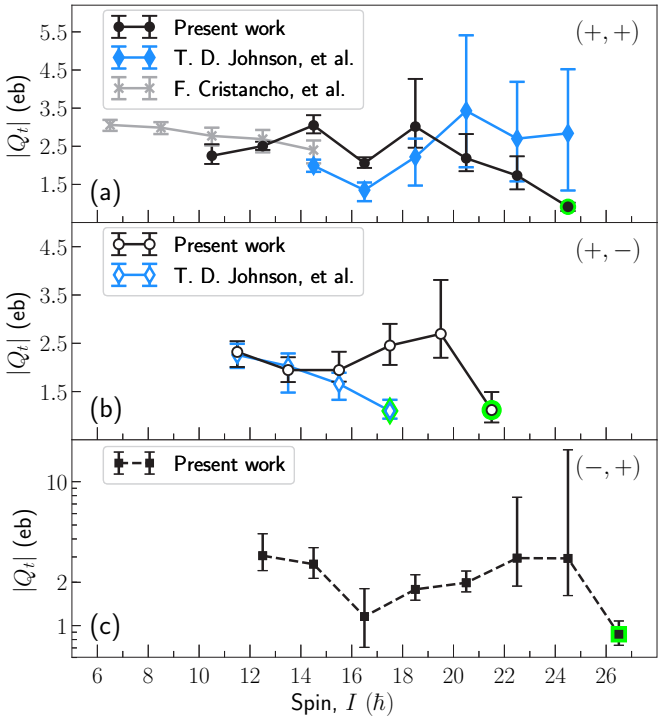

FIG. 5. Transition quadrupole moments determined from the lifetime measurements performed in this work together with previously reported values by Johnson *et al.* [5] and Cristancho *et al.* [3]. The light green circle indicates a lower limit for the quadrupole moment that was calculated using the effective lifetime.

for transitions of lower spin states of this band differ from our measurements, possibly due to the fact that the methodology applied in Refs. [3,5] to determine the lifetimes did not make use of the GFA technique, producing the possibility of getting imprecise values of lifetimes determined using the correlation method only. For the $(+,-)$ band the values reported in Ref. [5] are all in agreement with values reported here. All of the $|Q_t|$ values reported here for the $(-,+)$ band and shown in Fig. 5(c) were measured for the first time with the data analyzed in this work. Notice that the smallest value of $|Q_t|$ is found for the state at $(33/2^-)$ of the $(-,+)$ band. In Sec. IV a discussion on this $|Q_t|$ value will be given, and in Sec. V comparison with theoretical calculations will be made for all of the measured $|Q_t|$ values.

B. Side feeding times

The values obtained for the side-feeding times, which vary from values around 0.01 ps at high spins up to values close to 1 ps at low spins, are similar to values found for ^{84}Zr using the same reaction as in the experiment analyzed in this work [15]. These values are also similar to the values found for ^{82}Sr measured in the reaction ^{56}Fe(^{29}Si, $2pn$)^{82}Sr at 95 MeV [16].

To try to get an insight of the physics in the continuum, the side-feeding times were simulated by using the GAMMAPACE code [17]. The γ-ray transition probabilities are calculated from the product of the level density formula given in Ref. [18] with the γ-ray strengths. Statistical $M1$ and $E2$ transitions are considered with reduced transition probabilities $B(M1)_{\text{stat.}}$ and $B(E2)_{\text{stat.}}$. $E1$ statistical transitions are considered as giant dipole resonance transitions GDR with parameters calculated using the parametrization given in Ref. [19] which depends on the mass number A and the quadrupole deformation parameter β_2. In GAMMAPACE every point of the spin-energy plane has the possibility to be a member of a collective band in the continuum region. In the decay of these collective states the spread of the transition energies due to the rotational damping [20] was also considered. The side-feeding times are generated as the effective lifetime resulting from the decay chain feeding the state under study.

The input parameters given in Table III were used in GAMMAPACE for the simulation of the side-feeding times. The energy lost in the target was calculated using the SRIM code [11] and the pairing energy was computed from the difference between the binding energy of ^{83}Y and the average binding energy of the $A-1$ and $A+1$ neighboring nuclei. The properties of the collective transitions coming from the continuum depend on several parameters. The $\mathcal{J}^{(1)}$ value used in the GAMMAPACE simulation corresponds to the rigid rotor value to which all the discrete bands tend to converge. This value is related to the quadrupole deformation of the nucleus β_2, and therefore these two variables were fixed to the values given in Table III. On the other hand there is no argument for fixing the single-particle alignment i and the degree of collectivity of the transitions in the continuum. Therefore the different values of $B(E2)$ and i given in Table III were used for the simulations of the side-feeding times.

The simulated curves that best follow the experimental values are shown in Figs. 6 and 7. Note that the general tendency of the τ_{SF} values to increase when decreasing the spin is followed by both the simulated values and the experimental

TABLE III. GAMMAPACE input parameters used to simulate the side-feeding times.

^{32}S + ^{58}Ni at 135 MeV → ^{90}Ru → ^{83}Y + α + $3p$			
Statistical decay	GDR parameters		Quantities describing collective transitions in the continuum
$B(M1)_{\text{stat.}} = 0.01$ W.u.	$E_{G1} = 20.8$	$E_{G2} = 16.4$	$\beta_2 = 0.25$
$B(E2)_{\text{stat.}} = 1$ W.u.	$\Gamma_{G1} = 2.8$	$\Gamma_{G2} = 4.7$	$\mathcal{J}^{(1)} = 24.4\ \hbar^2$/MeV
	$\omega_1 = 0.3$	$\omega_2 = 0.7$	$B(E2) = 10, 40, 80$ W.u.
			$i(\omega) = 7.5, 2.5, 0.5\ \hbar$
Energy lost inside target = 8 MeV			Pairing energy $\Delta = 1.5$ MeV

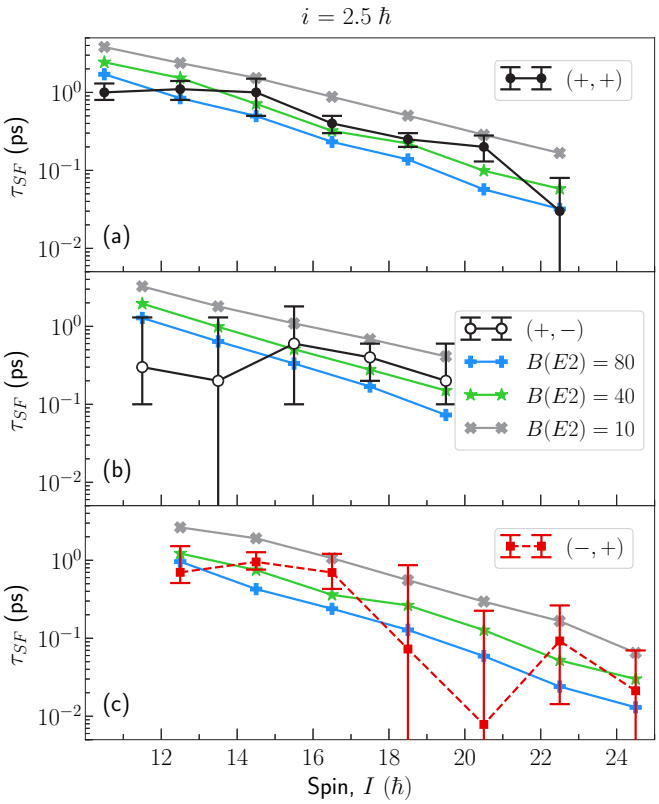

FIG. 6. Measured side-feeding times together with the values produced by simulations carried out using the GAMMAPACE code and assuming different values of the collective decay $B(E2)$ (in W.u.) while fixing $i = 2.5\ \hbar$. It can be seen that the $B(E2) = 80$ W.u. curves are the ones that best follow the experimental data for the three bands plotted.

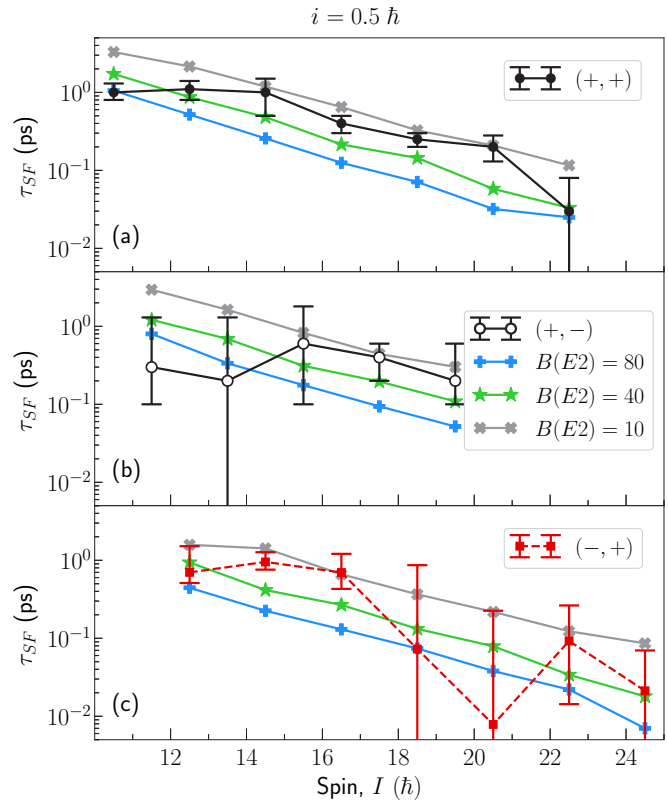

FIG. 7. Measured side-feeding times together with the values produced by simulations carried out using the GAMMAPACE code and assuming different values of the collective decay $B(E2)$ (in W.u.) while fixing $i = 0.5\ \hbar$. It can be seen that the $B(E2) = 40$ W.u. curves are the ones that best follow the experimental data the three bands plotted.

ones, considering the uncertainties. This tendency can be explained since the quasicontinuum states have properties similar to those of discrete states of similar spin. Among them the lifetimes of quasicontinuum states increase by decreasing the spin. Therefore the lower the spin of a discrete state, the more low spin values in the quasicontinuum contribute to their side-feeding times, increasing the resulting side-feeding time value.

From the simulated values, two sets were found to follow the experimental data similarly well for all of the three bands analized here. These values are shown in Table IV. Two conditions were examined for assigning the values of Table IV. (1) The curves for a given $B(E2)$ value follow the experimental data for all of the three bands analyzed. See for instance the curves in Fig. 7 with $B(E2) = 80$ W.u., which show larger distance than in Fig. 6 from the experimental data

TABLE IV. GAMMAPACE input parameters that best reproduce the experimental side-feeding times.

Set	$B(E2)$ (W.u.)	i ($\hbar$)	Fig.
1	80–40	2.5	6
2	40	0.5	7

for the (+, +) and (+, −) bands, although for the (+, −) band the curve seems to be a good approximation to the experimental data. (2) The simulated curves follow the experimental tendency all along the spin range. The latter was not the case for the $B(E2) = 10$ W.u. curves, which include the simulated points with the largest disagreement with the experiment. Such points appear at low spin values for which the simulation resulted in values up to four times larger than the experimental ones for the (+, +) and the (+, −) bands. From Table IV it can be said that either medium to high collective states with a medium single-particle alignment or medium collective states with no single-particle alignment are the physical scenarios for which the collective transitions from the continuum best reproduce the experimental data. It is important to notice that values different from the ones reported in Table IV can be ruled out since they do not reproduce the experimental values. Also the satisfactory results of the simulation using the values given in Table IV confirm that the values that were fixed in Table III were adequate. The agreement of experimental data with simulations shows that the theory used in Ref. [17] is consistent with the experimental results.

It is important to point out that this study, despite not representing a definitive description of the states coming from the continuum region, provides an insight into the physics of the

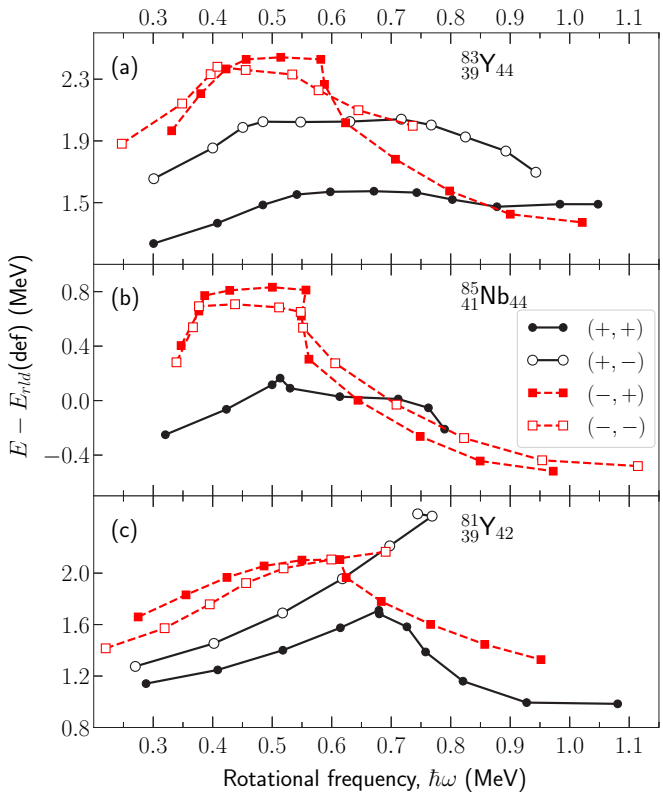

FIG. 8. Energy after subtracting the rotating liquid drop reference energy as function of rotational frequency. (a) Normally deformed bands of ^{83}Y. (b) Similar to (a) but for ^{85}Nb. (c) ^{81}Y. Panels (b) and (c) were produced with data from Refs. [25,26]. In all figures, positive and negative parity states are drawn by full and dashed lines, respectively. Closed (open) symbols are used for signature $\alpha = 1/2$ ($\alpha = -1/2$).

nucleus in the continuum. Nevertheless further experimental and theoretical studies are required to understand the behavior of the nuclei in the continuum region.

IV. CRANKED SHELL MODEL ANALYSIS

A. Comparisons with neighboring nuclei

The rotating liquid drop reference [21] can be calculated using the Lublin-Strasbourg drop (LSD) model [22], and will be denoted by $E_{\rm rld}$(def). The $E_{\rm rld}$(def) reference energy can be subtracted from the energy of the excited states to examine the relative variations of energy levels of different bands of the nucleus. A comparison of the $E - E_{\rm rld}$(def) quantity with the odd-Z even-N neighboring nuclei was performed. Among these nuclei $^{81}_{37}Rb_{44}$ presents two back-bendings in the negative parity bands, both at $\hbar\omega \approx 0.42$ MeV (see Refs. [23,24]), which makes this nucleus not suitable for the comparison with $^{83}_{39}Y_{44}$ in the $E - E_{\rm rld}$(def) quantity. Data for bands other than (+, +) in $^{85}_{39}Y_{46}$ are not available. For $^{85}_{39}Nb_{44}$ and $^{81}_{39}Y_{42}$ the $E - E_{\rm rld}$(def) quantity is shown in Figs. 8(b) and 8(c), where the data to produce the plots were taken from Refs. [25,26] respectively.

In Fig. 8 positive and negative parity states are drawn by full and dashed lines, respectively. Closed (open) symbols

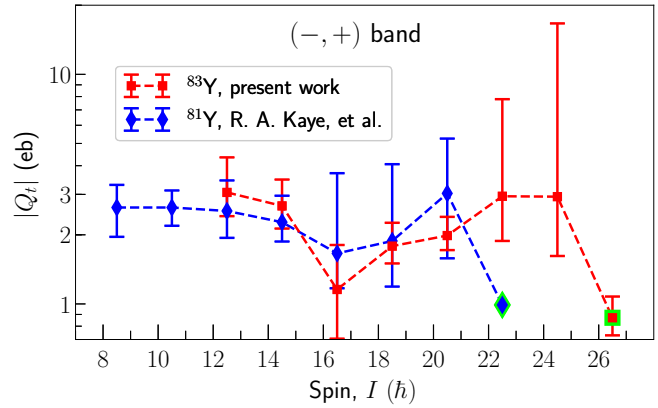

FIG. 9. Transition quadrupole moments determined for (−, +) bands of ^{81}Y [26] and ^{83}Y determined in this work.

are used for signature $\alpha = 1/2$ ($\alpha = -1/2$). This notation is adopted for all of the figures.

In Fig. 8(a), it can be seen that the relationship $E_{(+,+)} < E_{(+,-)} < E_{(-,+)} < E_{(-,-)}$ holds for the ^{83}Y curves at the lowest rotational frequency. The subsequent swaps from the initial energy relationship when increasing the spin will be examined. The term "signature inversion" will be used to indicate the case when the two signatures for a fixed parity cross. Signature inversion occurs for the negative parity bands at $\hbar\omega \approx 0.4$ MeV and the initial relation is recovered at $\hbar\omega \approx 0.6$ MeV. The negative parity (−, +) band swaps in energy with the positive parity band (+, +) for $\hbar\omega \approx 0.85$ MeV, as can be seen from Fig. 8(a). This swap appears also in the energy levels as a function of the spin, showing that at high spin states the yrast states belong to the (−, +) band. The latter means that none of the single bands drawn in Fig. 1 can be referred to individually as the yrast band. The relatively large energy reduction that the (−, +) band undergoes from $\hbar\omega \approx 0.58$ MeV, to cross and become more favored in energy than the (+, +) band [Fig. 8(a)], and its relationship with the $|Q_t|$ values, moment of inertia, and quasiparticle alignments, will be analyzed in Sec. IV B. Similar but less dramatic behavior is exhibited by the (−, −) band, whose energy starts to decrease from $\hbar\omega \approx 0.54$ MeV to take a value which is lower than the one for the (+, −) band at $\hbar\omega \approx 0.7$ MeV.

The curves of ^{85}Nb present behavior similar to the curves of ^{83}Y in Fig. 8. Signature inversion in the negative parity bands is present for both ^{85}Nb and ^{83}Y, as can be seen from Figs. 8(a) and 8(b). Likewise both nuclei present a remarkable change in the curve of the (−, +) band after the second band crossings at $\hbar\omega \approx 0.58$ and 0.56 MeV for ^{83}Y and ^{85}Nb respectively. Since the curves of $^{85}_{41}Nb_{44}$ resemble the ones of $^{83}_{39}Y_{44}$, it would be interesting to compare also with the $^{87}_{43}Tc_{44}$ isotone. However, only three transitions of the (+, +) band have been reported for ^{87}Tc. The remarkable change in the (−, +) band curve after the second band crossing at $\hbar\omega \approx 0.62$ MeV appears in ^{81}Y as well. Thus it is interesting to compare the quadrupole moments of the (−, +) band for ^{81}Y and ^{83}Y, which are shown in Fig. 9. No comparison with ^{85}Nb (−, +) band was possible since no quadrupole moments have been reported. At spin $I = 33/2$ a decrease in

$|Q_t|$ was found for the $(-,+)$ band of ^{83}Y. This spin coincides with the second band crossing. For ^{81}Y this lowering in $|Q_t|$ seems to appear as well. However, the $|Q_t|$ uncertainty does not allow us to confirm this tendency that, however, cannot be ruled out. In Sec. V theoretical calculations of several quantities including $E - E_{\rm rld}(\rm def)$ will be compared with the experimental values.

The evolution of measured $|Q_t|$ with the rotational frequency will be compared with the evolution of other physical quantities in Secs. IV B and IV C.

B. Negative parity bands

The ground configuration of the yrast band of the ^{82}Sr nucleus was used to obtain the Harris parameters [27] for the calculation of the reference spin I_g in the formula

$$I_g(\omega) = (\mathcal{J}_0 + \omega^2 \mathcal{J}_1)\omega + \ell. \quad (5)$$

The parameters found were

$$(\mathcal{J}_0, \mathcal{J}_1, \ell) = (23\ \hbar^2/\text{MeV},\ 0,\ -5\ \hbar). \quad (6)$$

Quasiparticle alignments $i(\omega)$ were determined as [28]

$$i(\omega) = I_x(\omega) - I_g(\omega), \quad (7)$$

where I_x is the angular momentum along the rotation axis. Figure 10 shows $|Q_t|$, the kinetic and dynamic moments of inertia $\mathcal{J}^{(1)}$ and $\mathcal{J}^{(2)}$, the quasiparticle alignment $i(\omega)$, and the relative energy to the rotating liquid drop reference $E - E_{\rm rld}(\rm def)$ as a function of the rotational frequency $\hbar\omega$ for the negative parity bands.

The kinetic moments of inertia, $\mathcal{J}^{(1)}$, in the region $A \approx 80$ converge to values between 20 and 25 $\hbar^2$/MeV [1], regardless whether they are even-even, odd-even, or odd-odd nuclei. The moment of inertia of the even-even nuclei increases with rotational frequency whereas that of odd-odd nuclei decreases. On the other hand odd-even nuclei show an intermediate behavior. Values shown in Figs. 10(c) and 11(c) are in agreement with this systematics.

Figure 10(b) shows two peaks in $\mathcal{J}^{(2)}$ for each band demonstrating the presence of the band crossings. For the $(-,+)$ band, calculations in Ref. [8] associate the first crossing at $\hbar\omega \approx 0.45$ MeV with protonic character. In Ref. [5] the proton alignment for the first crossing was also adopted. Since two consecutive decouplings of protons pairs are unlikely, the second crossing at $\hbar\omega \approx 0.58$ MeV was associated with the $\nu(g_{9/2})^2$ alignment scenario in Refs. [5,8]. In Sec. V B new calculations resulting in conclusions opposite to the ones in Refs. [5,8] will be discussed.

Figure 10(a) shows that the quadrupole moments for the $(-,+)$ band remain approximately constant for the entire range of rotational frequencies measured, except at $\hbar\omega \approx 0.58$ where the second band crossing appears. This band crossing is causing the sharpest and the largest effect on the quasiparticle alignment (increment of $\approx 3\ \hbar$) and the kinetic moment of inertia. The most notable change after this band crossing at $\hbar\omega > 0.58$ MeV is revealed by the $E - E_{\rm rld}(\rm def)$ quantity, which starts to decrease significantly, down to values even lower than those of the $(+,+)$ band [see Fig. 8(a)].

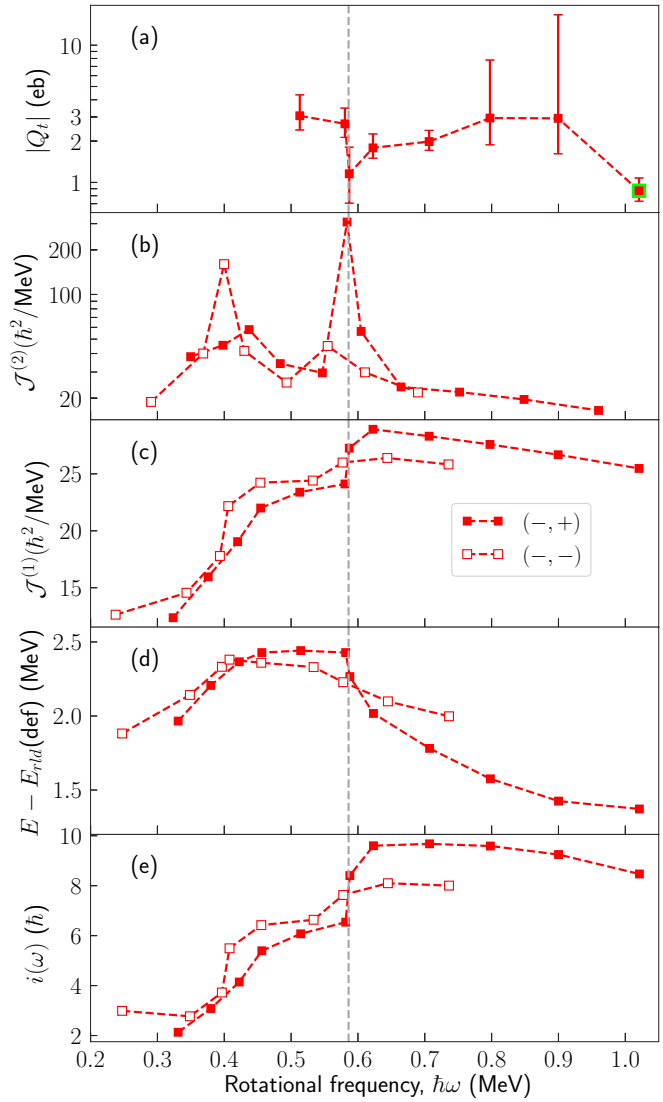

FIG. 10. Physical quantities describing the behavior of the ^{83}Y nucleus in its discrete states for the negative parity bands.

Band termination for the $(-,+)$ band has been suggested in Ref. [5] based in the single-particle alignment $i(\omega)$ of this band, which starts to decrease at $\hbar\omega \gtrsim 0.8$ MeV. However, no level lifetimes were measured before the present work for this band and no quadrupole moment values have been used to support the band termination interpretation. In Sec. V D terminating configurations in the bands analyzed here will be discussed.

C. Positive parity bands

Figure 11 shows the same physical quanties as in Fig. 10 but for the positive parity bands. Figure 11(b) shows the dynamic moment of inertia where band crossings can be observed. For these band crossings several suggestions have been provided. For the $(+,+)$ band the first crossing at $\hbar\omega \approx 0.55$ MeV was associated with the decoupling of a $g_{9/2}$ proton pair in Ref. [2]. Based on calculations and on the systematics, the scenario in which the $\nu(g_{9/2})^2$ alignment occurs first

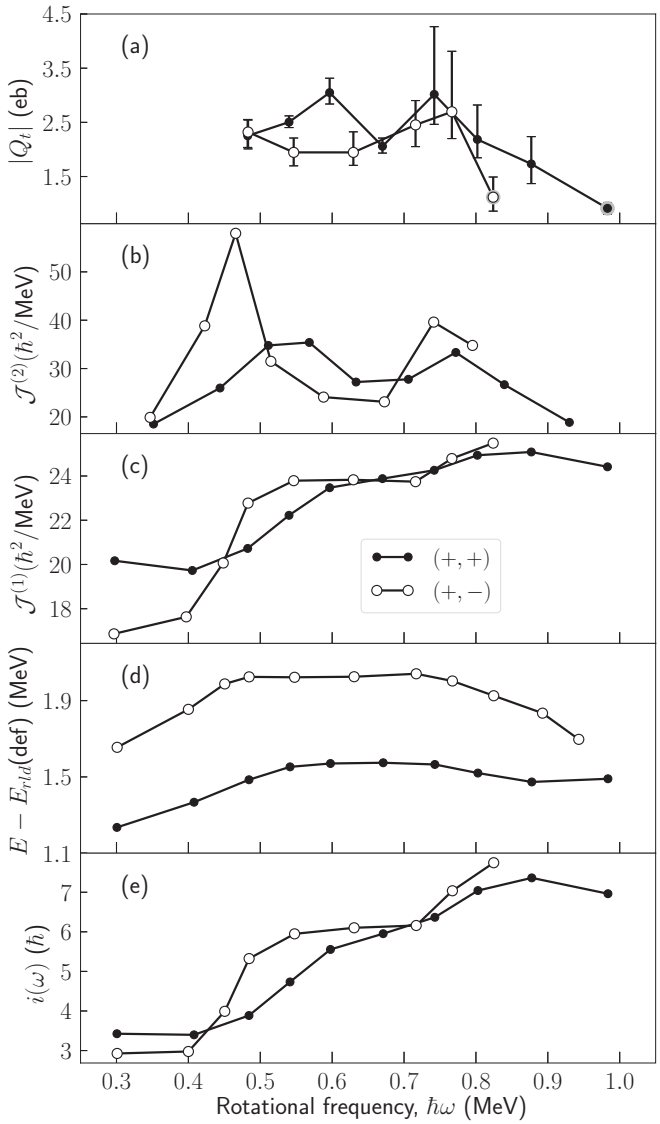

FIG. 11. Physical quantities describing the behavior of the ^{83}Y nucleus in its discrete states for the positive parity bands.

followed by $\pi(g_{9/2})^2$ alignment was the one adopted in Ref. [8] for both $(+,+)$ and $(+,-)$ bands.

Besides presenting the band crossings, Fig. 11 also shows that the $(+,+)$ band is the only one for which the quadrupole moments were measured before the first band crossing, which occurs at $\hbar\omega \approx 0.55$ MeV for this band. Notice that the frequency value of this crossing is the largest among the bands studied here, which made it possible to obtain measurements of quadrupole moments at rotational frequencies below the crossing. $|Q_t|$, $\mathcal{J}^{(1)}$, $i(\omega)$, and the $E - E_{\rm rld}$(def) quantities increase in the region below the crossing. This makes sense under the interpretation that the configuration before the crossing is just one valence proton. This valence proton being aligned along the rotation axis could be responsible for increasing both the moment of inertia and the quadrupole moment.

The following are common features found in Figs. 10 and 11:

(1) The general relationships between different quantities mean that band crossings which are manifested as peaks in $\mathcal{J}^{(2)}$ [panels (b)] come with relatively sharp increments of $\mathcal{J}^{(1)}$ and $i(\omega)$ in panels (c) and (e) respectively; a general behavior which is illustrated in our analysis of the ^{83}Y bands.

(2) The quantities $E - E_{\rm rld}$(def) of panels (d) and the kinetic moment of inertia $\mathcal{J}^{(1)}$ in panels (c) start to saturate right after the first band crossings.

V. CNS AND CNSB CALCULATIONS

Calculations on ^{83}Y have been carried out in the CNSB (cranked Nilsson-Strutinsky-Bogoliubov) and CNS (cranked Nilsson-Strutinsky) formalisms. The CNS model is defined in [21,29,30]. The CNSB model is based on ULTIMATE CRANKER, which was developed by Bengtsson [31]. The formalisms in the present calculations are defined in Refs. [32,33]. $A = 80$ parameters have been used [30]. In the CNS formalism the configurations are labeled as $[p_1p_2, n_1n_2]$ or in shorter form as $[p_2, n_2]$. Here p_1 (n_1) is the number of holes in the $Z = (N =)\,40$ core while p_2 (n_2) is the number of $g_{9/2}$ protons (neutrons). For the different groups the signature is often specified by a subscript when not equal to zero: "+" for $\alpha = 1/2$ and "−" for $\alpha = -1/2$. The only quantum numbers which are preserved in the CNSB formalism are parity and signature for protons and neutrons, i.e., configurations are specified as $(\pi_p, \alpha_p)(\pi_n, \alpha_n)$. The Q_t value is calculated from the deformation as defined in Ref. [34] and references therein.

A. CNS assignments

The observed bands of ^{83}Y are drawn relative to the rotating liquid drop energy in Fig. 12(a). It is instructive to compare with unpaired CNS calculations to get a general understanding of these bands. Thus, the low-lying calculated configurations which can be assigned to these bands are drawn relative to the same reference in Fig. 12(b). In addition to the collective bands drawn in Fig. 12(b), the [1,6] bands are calculated less than 0.5 MeV above yrast for low spin values up to $I \approx 15$, but no other collective bands are calculated within a range of 1 MeV above yrast. Thus, it seems well established that the configurations in Fig. 12(b) should have a major contribution to the wave functions of the observed bands, except for the possibility of a large contribution from the [1,6] configuration in the positive parity bands at low spin values.

The calculated γ deformation for all the configurations in Fig. 12(b) is in the range $[-40°, -60°]$, i.e., close to collective rotation at oblate shape. The ε_2 deformation is in the range $\varepsilon_2 = [0.25, 0.30]$ for low spin values, reaching $\varepsilon_2 \approx 0.15$ at high spin but with no termination in a noncollective state. The single-particle orbitals for protons are drawn at a typical deformation in Fig. 13. The proton and neutron orbitals are similar, so, in order to get a general understanding, this diagram can be used also for neutrons. Then it is clear that the neutron configuration with six $g_{9/2}$ neutrons is most favored from low to high frequencies, and this is also the configuration for all bands drawn in Fig. 12(b). There is a

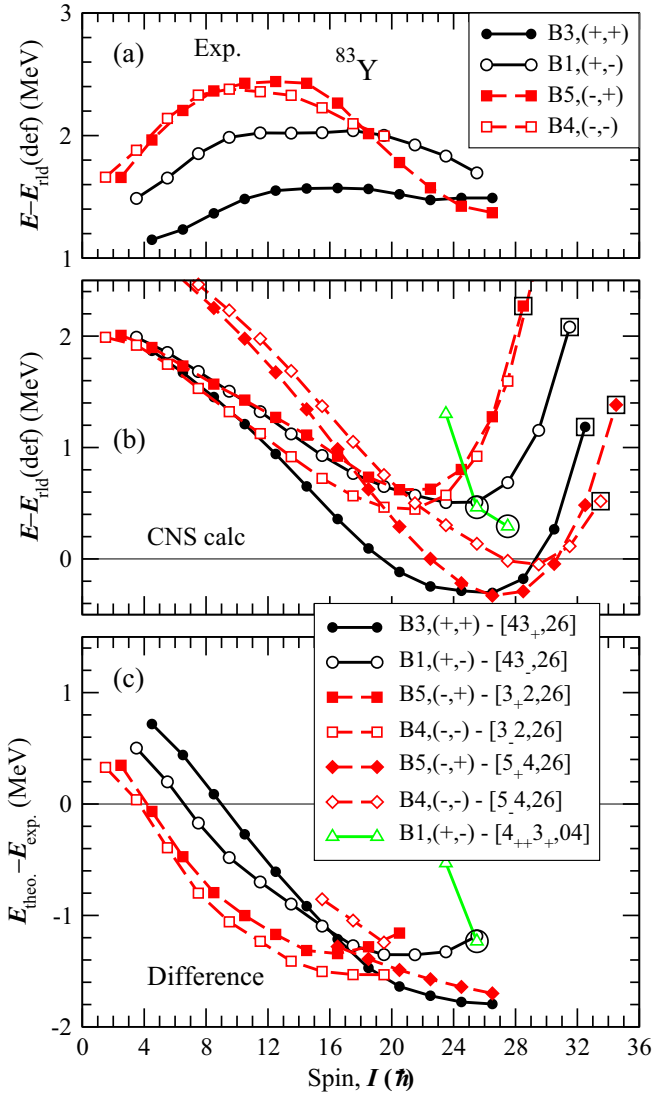

FIG. 12. Comparison between experiment and CNS calculations. (a) Observed bands drawn relative to the rotating liquid drop reference. (b) Calculated configurations assigned to the experimental bands. (c) Difference between calculations and experiment. States which are calculated to be fully aligned are encircled while large squares are used for states which have reached the I_{max} value of their configuration, but which are still collective.

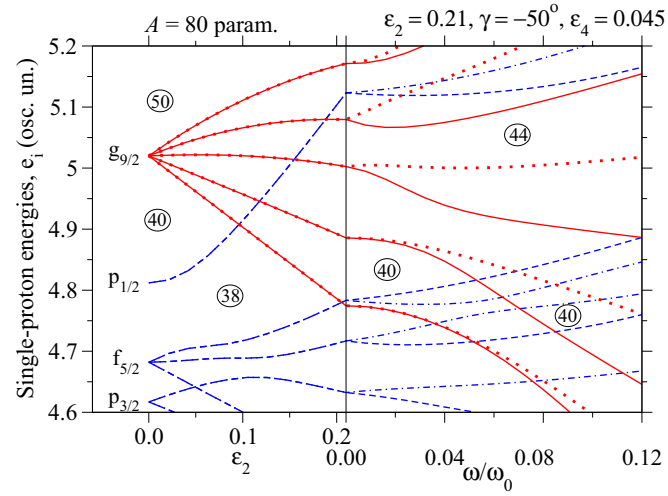

FIG. 13. Proton single-particle orbitals at a typical deformation for the configurations assigned to the observed bands in ^{83}Y, $\varepsilon_2 = 0.21$, $\gamma = -50°$, $\varepsilon_4 = 0.045$. In the left part of the diagram, the ε_2 and ε_4 deformations increase linearly up to 0.21 and 0.045, respectively, at a constant value of $\gamma = -50°$, while the single-particle Routhians are shown as a function of the rotational frequency at constant deformation in the right part.

higher level density around particle number 39, and the figure suggests the configurations with two or three $g_{9/2}$ protons are favored at low or intermediate spin and maybe with four $g_{9/2}$ protons at the highest spin values. Indeed, it is these configurations which are assigned to the observed bands, i.e., [3,6] to the positive parity bands and [2,6] and [4,6] at low and high spin, respectively, for the negative parity bands. With these assignments, experiment and calculations are compared in Fig. 12(c). The comparison comes out more or less as expected, i.e., the differences are collected within a range of ±0.5 MeV, where the average difference increases with decreasing spin as expected because of an increasing pairing energy. The fluctuations around the average value should then be understood from different pairing energies in different configurations, but certainly also from the general uncertainty in the calculations.

For the observed bands, there is a clear tendency that the unfavored branch of the positive parity band approaches the favored branch at high spin. This is clearly in disagreement with the calculations presented in Fig. 12(b). The large calculated signature splitting is easily understood from Fig. 13, where the second $g_{9/2}$ orbital shows a large and increasing signature splitting. Thus, it can be energetically advantageous to put the third $g_{9/2}$ proton in the favored signature instead, and then let the two highest $N = 4$ protons have the same signature; see Fig. 13. These configurations, labeled [4$_{++}$3$_+$, 26] and [4$_{--}$3$_+$, 26], are calculated slightly lower in energy at high spin than the [43$_-$, 26] configuration drawn in Fig. 12(b). A related possibility is to close the $N = 40$ core, i.e., with four $g_{9/2}$ neutrons, still with the favored signature for the odd $g_{9/2}$ proton and with the same signature for the highest $N = 4$ protons. This possibility is illustrated in Fig. 12(b) by the configuration labeled [4$_{++}$3$_+$, 04]. It leads to aligned states for $I = 25.5, 27.5$ which are relatively favored in energy.

B. CNSB calculations

With the CNS calculations as background, the observed bands are now compared with calculations including pairing in Fig. 14. We note that the differences between calculations and experiment are now essentially constant on average. On the other hand, the spread of the differences is still similar and about as large as for the unpaired calculations, i.e., in an approximate range of ±0.5 MeV. This suggests that the unpaired configuration labeling is more or less valid also with pairing included. Consequently, the positive parity bands

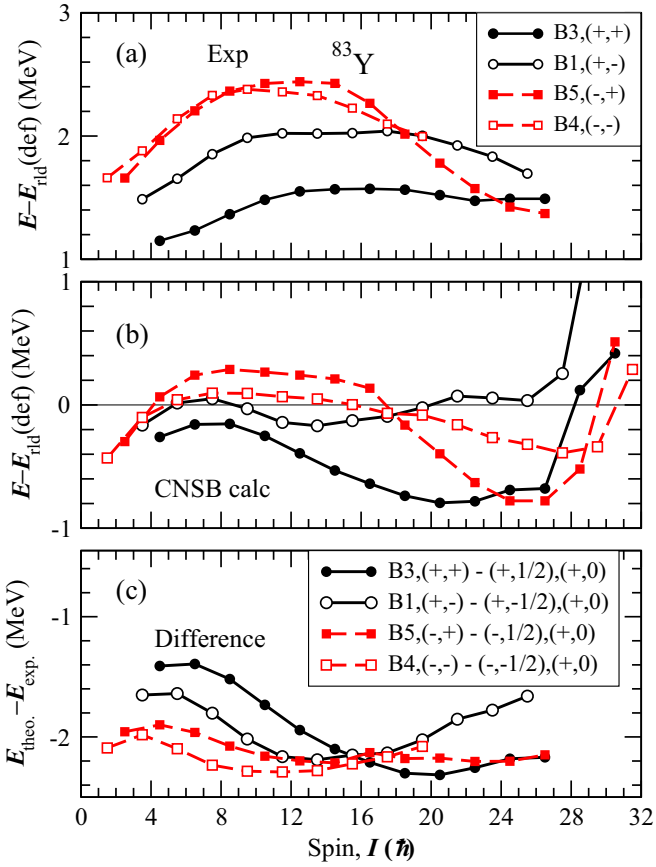

FIG. 14. Comparison between experiment and CNSB calculations. Note that only signature and parity for protons and neutrons are specified for the calculated bands, in contrast to the CNS calculations in Fig. 12(b) where the configurations are specified in more detail.

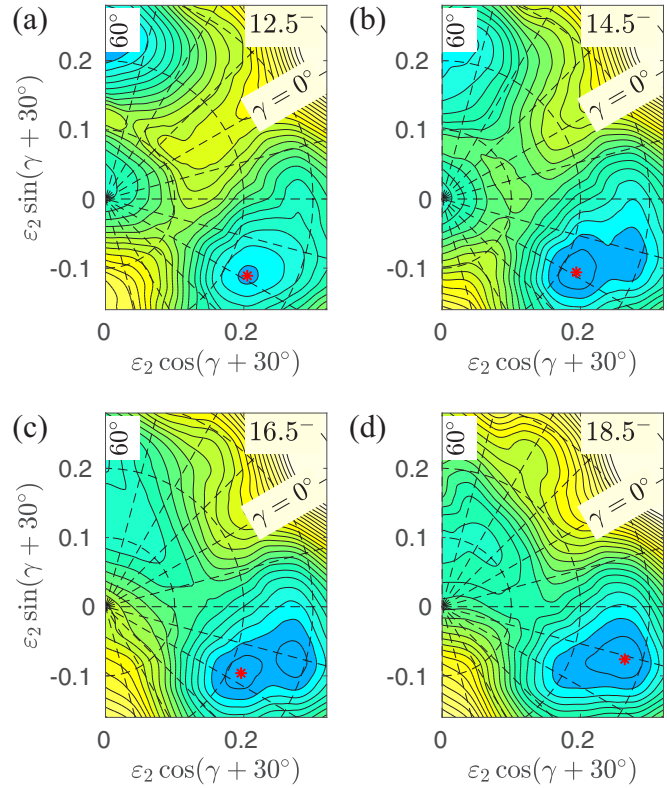

FIG. 15. Calculated total energy surfaces for the $(-, 1/2)(+, 0)$ configuration in the CNSB formalism illustrating the states before and after the second band crossing. The contour line separation is 0.2 MeV. The general minima are indicated by a red asterisk in each of the figures.

can be labeled as $\pi(g_{9/2})^3\nu(g_{9/2})^6$ in their full spin range or possibly as $\pi(g_{9/2})^1\nu(g_{9/2})^6$ at low spin; see the discussion above. However, they go through a band crossing around $I = 11$ ($\hbar\omega = 0.45$ MeV), which shows up in a similar way also in the negative parity bands [see Figs. 10(b) and 11(b)]. This suggests that the crossing is caused by a similar mechanism for both parities. Thus, the crossing is probably caused by the neutrons because the neutron configuration $(g_{9/2})^6$ is common for both parities. Furthermore, because the calculated shape is close to oblate, it is difficult to align a few high-j particles, i.e., it is much more difficult to align two or three $g_{9/2}$ protons than to align six $g_{9/2}$ neutrons. The difficulty to align the protons is also seen in the CNS calculations, where, for the [2,6] configuration, the spin contribution from the $g_{9/2}$ protons is much smaller than that from the $g_{9/2}$ neutrons. Furthermore, in the CNSB calculations the g factor indicates that the spin is mainly built from the neutrons just after the crossing and the neutron pairing delta is seen to drop for spin values $I \approx 10$, while the proton delta remains more constant. Thus, all these considerations indicate that the alignment for $I \approx 10$ is caused by the neutrons, which is in contrast to the conclusions in Refs. [5,8].

For negative parity, there is a second crossing just below $I = 20$ which shows up in a similar way in the paired and unpaired calculations, indicating that it is caused by a crossing between unpaired configurations, in this case between the $\pi(g_{9/2})^2$ and $\pi(g_{9/2})^4$ configurations with no change of the neutron configuration, $\nu(g_{9/2})^6$. Note also that before the crossing, signature $\alpha = -1/2$ is favored in both experiment and calculations. After the crossing, the experimental bands appear to go through a signature crossing, although the $\alpha = -1/2$ band is not seen at spins high enough to show this clearly. In any case, such a crossing is supported both by the CNS and the CNSB calculations. The fact that the crossing is mainly caused by such a configuration change also when pairing is added is seen from the energy surfaces. In the unpaired calculations, the deformation will become larger the more particles are excited across the 40 gap; i.e., for the same spin value, the deformation is considerably larger in the $\pi(g_{9/2})^4$ than in the $\pi(g_{9/2})^2$ configuration. The same deformation change is seen in CNSB calculations where energy surfaces for the $(-, 1/2)(+, 0)$ configuration are plotted in Fig. 15. For the 12.5^- state the minimum around $\gamma = -50°$ is calculated at a relatively small deformation, which roughly agrees with the deformation calculated for the $[3_+2, 26]$ configuration in CNS. Then for the 14.5^- and 16.5^- states where the $[3_+2, 26]$ and $[5_+4, 26]$ configurations come close together, two coexisting minima are seen at similar energies. For the 18.5^- state, where the $(g_{9/2})^4$ configuration is clearly lowest in the CNS calculations, the larger deformation minimum

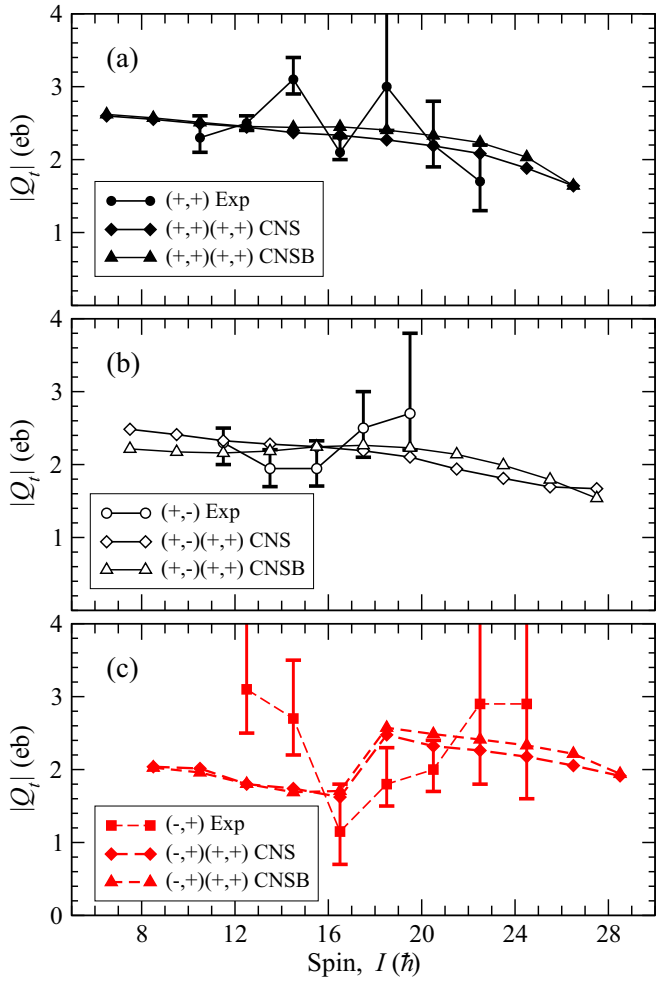

FIG. 16. Comparison between observed $|Q_t|$ values and values obtained from calculated deformations along the collective trajectories in calculations including (CNSB) and neglecting (CNS) pairing correlations.

becomes lower in energy. The fact that two coexisting minima are clearly seen in the CNSB calculations shows that, even with pairing included, the two configurations can be clearly distinguished and they are not strongly mixed.

C. The transitional quadrupole moment

The transitional quadrupole moments Q_t are now calculated from the deformations along the trajectories of the collective bands and compared with experiment in Fig. 16. The fact that the calculated values with and without pairing come close together is another indication that the wave functions are rather similar and thus that the more detailed configuration labeling used in the CNS calculations is approximately valid also in the CNSB calculations. Especially, the configuration change from $\pi(g_{9/2})^2$ to $\pi(g_{9/2})^4$ in the negative parity at $I \approx 18.5$ shows up in very much the same way in the CNS and CNSB calculations.

In general, it is expected that, at band crossings and configuration changes, the $B(E2)$ values and thus Q_t should be smaller. It is therefore gratifying that, at the configuration change of the $(-,+)$ band at $I \approx 16$, the experimental $|Q_t|$ appears to be particularly small. Then for the $(+,-)$ band the fluctuations appear smaller and, considering the error bars, the values of $|Q_t|$ may very well follow a continuous curve as suggested by the calculations. For the $(+,+)$ band on the other hand, the fluctuations are more accentuated and cannot be explained by some band crossing. One possibility is that the aligned noncollective states could mix into the collective bands and then have a large influence on the $|Q_t|$ values. The discontinuities in the bands which are seen, e.g., from the $\mathcal{J}^{(2)}$ moments of inertia are consistent with such a mixing.

The question is then if there are any low-lying noncollective states which could mix into the collective bands. Thus, in Fig. 18, the lowest energy states of small or no collectivity are compared with the collective bands. The figure suggests that these noncollective states can become competitive for several spin values in the different bands. It has been noticed before that pairing tends to favor the noncollective states [33], and this is the case also for the present calculations on ^{83}Y. This is seen from a comparison between total energy surfaces shown with and without pairing in Figs. 17(a) and 17(b) respectively. A general feature is that the maxima or ridges between become lower with pairing included, which just shows the well-known feature that the pairing energy is larger in a region with a high level density, i.e., in regions with a positive shell energy and thus a high total energy. Apart from this, the general impression is, however, that the surfaces in the two figures are very similar. It is also evident that the aligned states are relatively lower in energy by typically a few hundred keV in the surfaces with pairing included. This is true both for the larger deformation aligned states at $\varepsilon_2 \approx 0.20$–$0.25$ and the smaller deformation states at $\varepsilon_2 \approx 0.10$. Consider for example $I = 16.5$, where, as seen in Fig. 18(a), the aligned state is close in energy to the collective state. This is also seen in the surface in Fig. 17(a), while the $\gamma = 60^\circ$ minimum is more than 0.5 MeV above the collective minimum in Fig. 17(b). The noncollective configuration corresponds to $\pi(g_{9/2})^1\nu(g_{9/2})^4$, i.e., [21,04], where the spin is built from the full alignment of the $g_{9/2}$ particles, $I = 4.5 + 12 = 16.5$. In this case we note that it is exactly at the spin value with a low-energy aligned state, $I = 16.5$, that the observed Q_t in the $(+,+)$ band has a relatively low value.

D. Possible band terminations

It is concluded in Ref. [5] that there is no evidence that the $(+,+)$ band should terminate in a noncollective state. Indeed all of the the bands which are drawn in Fig. 12(b) are not terminating in a noncollective state. The spin in these configurations is limited, with a value of $I_{\max}$ which is not much larger than the presently observed highest spin values. This appears consistent also with the present measurements of Q_t. Indeed, the collective configurations show some very interesting features when they approach their $I_{\max}$ values. Thus, as seen in Fig. 12(b), the energies of these configurations are calculated to increase strongly when they approach $I_{\max}$, where the $E - E_{\rm rld}$ curves resemble, e.g., the curves of the smooth terminating bands in the $A = 110$ region [30].

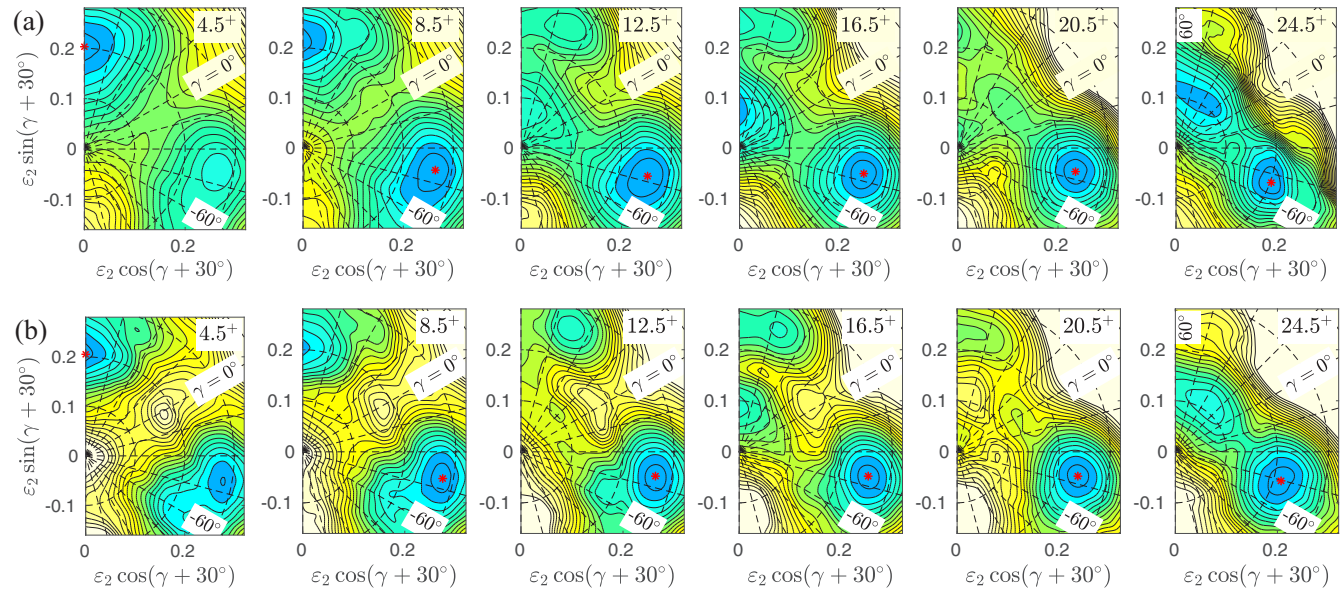

FIG. 17. Calculated total energy surfaces for $(+,1/2)(+,0)$ configurations. The contour line separation is 0.2 MeV. (a) Energy surfaces calculated in the CNSB formalism, i.e., with pairing included. (b) Energy surfaces calculated in the CNS formalism, i.e., with no pairing energy. The general minima are indicated by a red asterisk in each of the figures.

Furthermore, such an energy increase has been observed experimentally in the neighbor nucleus ^{84}Zr, where the ground band has been identified [35] to the maximum spin, $I = 34$, of the configuration which is assigned [15] to this band, [4,6]. Note especially that the strong increase of $E - E_{\rm rld}$ was predicted before it was observed; see, e.g., Fig. 12 of Ref. [15]. A closer study of these configurations show that they remain collective when they reach their $I_{\rm max}$ values, i.e., they can be described as nonterminating bands [36]. The different configurations are drawn to their $I_{\rm max}$ values in Fig. 12(b). Currently the states of the band 3 have been observed three transitions short of its maximum spin state and the other bands have been observed even further away from termination. Band 3 is built in the configuration

$$\pi\left[(pf)_6^{-4}(g_{9/2})^3_{10.5}\right]_{16.5}\nu\left[(pf)_4^{-2}(g_{9/2})^6_{12}\right]_{16}, \qquad (8)$$

which is defined relative to a ^{80}Zr core and where the subscripts represent the maximum spin within the configurations, i.e., $I_{\rm max} = 16.5 + 16 = 32.5$. The fact that the corresponding band in ^{84}Zr has been observed to its $I_{\rm max}$ value suggest that this should be possible also for these bands in ^{83}Y. Indeed, as discussed in Ref. [36] it should in principle be possible to observe even the $I_{\rm max} + 2$ state, but it will lie very high above yrast. Thus, in Fig. 12(b), these bands have not been followed beyond their $I_{\rm max}$ values.

While the observed collective bands are not expected to show any real terminations, this might be the case for other configurations with fewer particles excited across the semimagic gap at particle number 40. Thus, in Fig. 18, some states of this kind are seen. The low-lying positive parity $I = 16.5$ state is interesting because it can be described as the $I_{\rm max}$ state of the configuration with one proton and four neutrons outside a ^{78}Sr core; see Fig. 19. The ^{78}Sr core is used because it will correspond to a proton configuration with no particles in the $p_{1/2}$ orbitals which will thus not give any spin contribution.

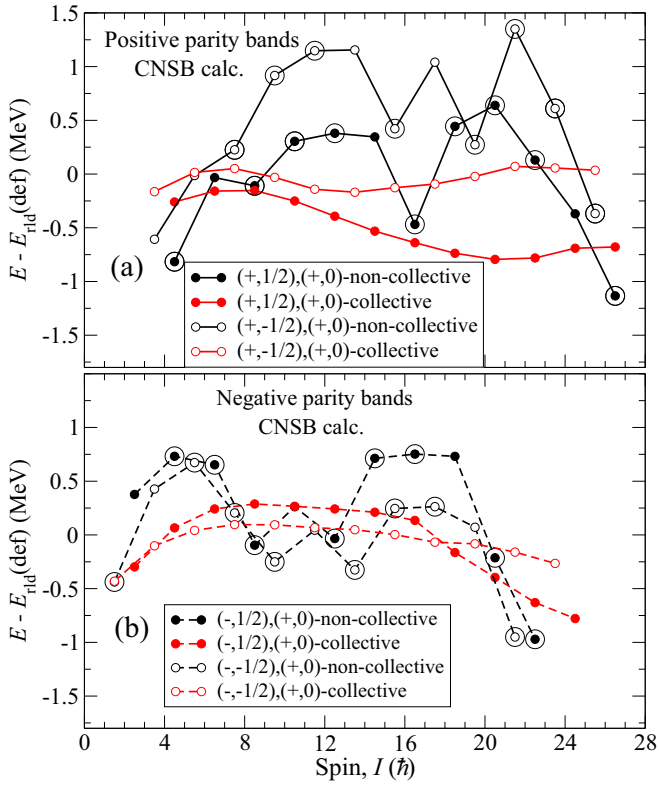

FIG. 18. Comparison between the collective bands and the lowest energy configurations at or in the vicinity of the noncollective limit at $\gamma = 60°$. States on the noncollective axis are encircled.

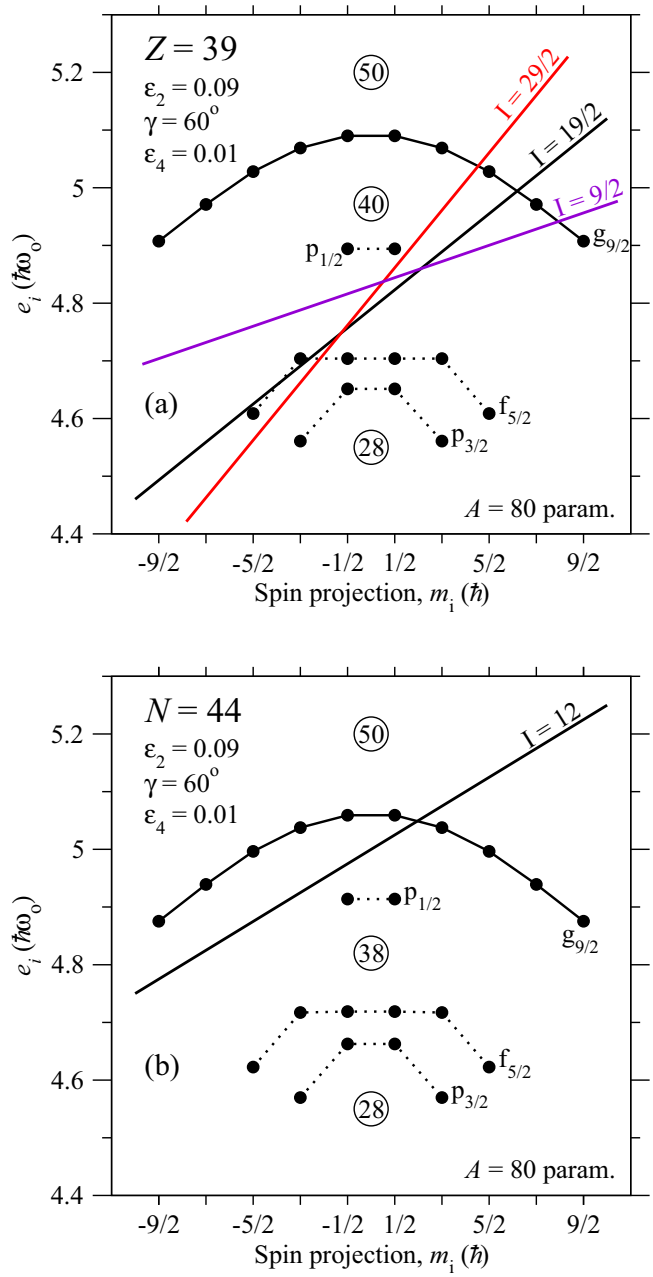

FIG. 19. Single-particle proton (a) and neutron (b) energies, e_i, as a function of the spin projection, m_i. The lines indicate the Fermi levels producing the spin labeled that describes the configurations of the 16.5^+, 26.5^+, 21.5^-, and 22.5^- states. Starting from the $I = 19/2$ proton state, an $I = 21/2$ state which is almost as favored in energy is formed if the fp hole is placed in the $m_i = -5/2$ state instead of the $m_i = -3/2$ state. In the configuration for the aligned $I = 22.5^-$ state in Fig. 18(b), this proton state is combined with the $I = 12$ neutron state.

Some other interesting aligned states in Fig. 18 are the negative parity states at $I = 21.5, 22.5$ and the positive parity $I = 26.5$ state. They can be described as having one hole and two holes, respectively, in a ^{78}Sr core. All these states are related to the [2,4] configuration in ^{84}Zr, which terminates at $I = 20$ [15]. Compared with this aligned 20^+ state, the 16.5^+ state has one less $g_{9/2}$ proton, the 21.5^-, 22.5^- states have one more pf hole, while the 26.5^+ state corresponds to a two-hole, one-particle excitation relative to the $I = 20$ state. All of these configurations terminate in their maximum spin states at a relatively small oblate deformation, $\varepsilon_2 \approx 0.09$. Comparing with experiment, the side band to the $(-,+)$ observed to a tentative $I = 22.5$ state in Ref. [5] might be assigned to the configuration terminating at $I = 22.5$. Furthermore, the highest spin state in the $(+,+)$ band is observed somewhat lower in energy, which might be caused by an interaction with the terminating 26.5^+ state.

For negative parity, there are several low-lying noncollective states for $I = 8.5$–13.5 [see Fig. 18(b)]. These are formed at $\varepsilon \approx 0.22$ ($\gamma = 60°$) in the same [2,6] configurations as the collective bands, but with several antialigned spin vectors.

VI. SUMMARY AND CONCLUSIONS

The measured level lifetimes and side-feeding times follow the inequality $\tau_{SF} \gtrsim \tau$, and comparisons of the side-feeding times with GAMMAPACE simulations resulted in $B(E2)$ values in the range 40–80 W.u. for the collective transitions in the continuum region. This indicates that the theory used in GAMMAPACE for the simulation of the transitions in the continuum region may be a good approach to the description of the decay in that region.

The transitional quadrupole moments of high spin states of three normally deformed bands of ^{83}Y were measured and their evolution with rotational frequency was compared with other physical quantities. As a result it was found that the smallest measured $|Q_t|$ value appears at the sharpest band crossing among the bands studied, namely the second crossing in the $(-,+)$ band. Contrary to what was previously assigned in Refs. [5,8], this band crossing was associated with a change between $\pi(g_{9/2})^2$ and $\pi(g_{9/2})^4$ configurations, which is manifested in an increase of the deformation. Figure 9 shows that the $|Q_t|$ values for the $(-,+)$ band in ^{81}Y and ^{83}Y are equivalent within uncertainties, where both exhibit a minimum value at the second band crossing. It was also shown that the measured $|Q_t|$ values for the $(+,+)$ and the $(-,+)$ bands are similar to those previously measured. Cranked Nilsson-Strutinsky calculations with (CNSB) and without (CNS) inclusion of pairing correlations are in general agreement with the measured values, where the few values that fall outside the uncertainties could be explained by two possible scenarios: (1) a possible mixing with noncollective states and (2) the introduction of nonvalid correlations induced by a lifetime obtained gating from below only and thus possibly impacting also the values for lower spin.

CNS calculations were carried out and used to specify the configurations in the CNSB formalism from which the normally deformed bands of ^{83}Y were studied. Three facts supported that the CNS assignments are approximately valid also for the CNSB formalism: (1) The spread of the difference between the experimental $E - E_{\rm rld}$ energies and those calculated for both the CNS and the CNSB formalisms is within a range of 0.5 MeV [see Figs. 12(c) and 14(c)]. (2) The calculated Q_t are very similar in the two formalisms, Fig. 16. (3) The energy surfaces are very similar, Fig. 17.

The calculations indicate that the observed bands will not terminate if their I_{max} values are reached (nontermination). The absence of termination is in agreement with the conclusions of Ref. [5] for the $(+,+)$ band but in contrast to what was concluded for the $(-,+)$ band. On the other hand other configurations with fewer particles excited across the $Z = 38$ and $N = 40$ gaps were calculated to terminate and were compared with similar structures in ^{84}Zr and one sideband of ^{83}Y reported in Ref. [5].

ACKNOWLEDGMENTS

W.R. acknowledges partial support from Colciencias, Contract No. 617 "Becas doctorados nacionales." This work was supported in part by the US National Science Foundation under Grants No. PHY-9523974 and No. PHY-9970991 (FSU). We thank M. Devlin, I. Y. Lee, and A. O. Macchiavelli for their contribution to the satisfactory execution of the experiment.

[1] S. L. Tabor, Phys. Rev. C **45**, 242 (1992).
[2] C. J. Lister, B. J. Varley, W. Fieber, J. Heese, K. P. Lieb, E. K. Warburton, and J. W. Olness, Z. Phys. A **329**, 413 (1988).
[3] F. Cristancho, K. P. Lieb, J. Heese, C. J. Gross, W. Fieber, T. Osipowcz, and S. Ulbig, Nucl. Phys. A **501**, 118 (1989).
[4] T. D. Johnson, F. Cristancho, C. J. Gross, M. Kabadiyski, K. P. Lieb, D. Rudolph, M. Weiszflog, T. Burkardt, J. Eberth, and S. Skoda, Z. Phys. A **347**, 285 (1994).
[5] T. D. Johnson, A. Aprahamian, C. J. Lister, D. Blumenthal, B. Crowell, P. Chowdury, P. Fallon, and A. Machiavelli, Phys. Rev. C **55**, 1108 (1997).
[6] D. G. Sarantites, P. Hua, M. Devlin, L. Sobotka, J. Elson, J. Hood, D. LaFosse, J. Sarantites, and M. Maierb, Nucl. Instrum. Methods Phys. Res. A **381**, 418 (1996).
[7] I.-Y. Lee, Nucl. Phys. A **520**, c641 (1990).
[8] F. Cristancho, C. J. Gross, K. P. Lieb, D. Rudolph, O. Skeppstedt, M. A. Bentley, W. Gelletly, H. G. Price, J. Simpson, J. L. Durell, B. J. Varley, and S. Rastikerdar, Nucl. Phys. A **540**, 307 (1992).
[9] D. A. Torres, N. De La Rosa, F. Cristancho, S. L. Tabor, R. A. Kaye, G. Z. Solomon, J. Döring, G. D. Johns, M. Devlin, F. Lerma, D. G. Sarantites, I.-Y. Lee, A. O. Macchiavelli, and A. Garzón, in *XXXV Brazilian Workshop on Nuclear Physics*, 2–6 September 2012, São Sebastião, São Paulo, Brazil, edited by F. L. Melquiades, F. A. Genezini, N. H. Medina, R. M. dos Anjos, and S. dos Santos Avancini, AIP Conf. Proc. No. 1529 (AIP, New York, 2013) p. 170.
[10] A. Garzón, W. Rodriguez, F. Cristancho, and M. Tao, Comput. Phys. Commun., 106854 (2019).
[11] J. Ziegler, J. Biersack, and M. Ziegler, SRIM, the Stopping and Range of Ions in Matter, SRIM Company, 2008.
[12] J. Blatt and V. Weisskopf, *Theoretical Nuclear Physics* (Dover, Mineola, NY, 2012).
[13] R. Casten, *Nuclear Structure from a Simple Perspective* (Oxford University Press, Oxford, 2000).
[14] W. Nazarewicz and I. Ragnarsson, in *Handbook of Nuclear Properties*, edited by D. Poenaru and W. Greiner (Clarendon, Oxford, 1996).
[15] R. Cardona, F. Cristancho, S. L. Tabor, R. A. Kaye, G. Z. Solomon, J. Döring, G. D. Johns, M. Devlin, F. Lerma, D. G. Sarantites, I.-Y. Lee, A. O. Macchiavelli, and I. Ragnarsson, Phys. Rev. C **68**, 024303 (2003).
[16] S. L. Tabor, J. Döring, J. W. Holcomb, G. D. Johns, T. D. Johnson, T. J. Petters, M. A. Riley, and P. C. Womble, Phys. Rev. C **49**, 730 (1994).
[17] F. Cristancho and K. P. Lieb, Nucl. Phys. A **524**, 518 (1991).
[18] D. W. Lang, Nucl. Phys. **77**, 545 (1966).
[19] G. A. Leander, Phys. Rev. C **38**, 728 (1988).
[20] B. Lauritzen, T. Døssing, and R. Broglia, Nucl. Phys. A **457**, 61 (1986).
[21] B. G. Carlsson and I. Ragnarsson, Phys. Rev. C **74**, 011302(R) (2006).
[22] K. Pomorski and J. Dudek, Phys. Rev. C **67**, 044316 (2003).
[23] S. L. Tabor, P. D. Cottle, C. J. Gross, U. J. Hüttmeier, E. F. Moore, and W. Nazarewicz, Phys. Rev. C **39**, 1359 (1989).
[24] J. Döring, R. Schwengner, L. Funke, H. Rotter, G. Winter, B. Cederwall, F. Lidén, A. Johnson, A. Atac, J. Nyberg, and G. Sletten, Phys. Rev. C **50**, 1845 (1994).
[25] K. Jonsson, B. Cederwall, A. Johnson, R. Wyss, T. Bäck, J. Cederkäll, M. Devlin, J. Elson, D. R. LaFosse, F. Lerma, D. G. Sarantites, R. M. Clark, I. Y. Lee, A. O. Macchiavelli, and R. W. Macleod, Nucl. Phys. A **645**, 47 (1999).
[26] R. A. Kaye, C. T. Rastovski, S. L. Tabor, J. Döring, F. Cristancho, M. Devlin, G. D. Johns, I. Y. Lee, F. Lerma, A. O. Macchiavelli, D. G. Sarantites, and G. Z. Solomon, Phys. Rev. C **66**, 054305 (2002).
[27] R. Bengtsson and S. Frauendorf, Nucl. Phys. A **327**, 139 (1979).
[28] H. Ejiri and J. de Voigt, *Gamma-ray and Electron Spectroscopy in Nuclear Physics* (Clarendon, Oxford, 1989).
[29] T. Bengtsson and I. Ragnarsson, Nucl. Phys. A **436**, 14 (1985).
[30] A. V. Afanasjev, D. B. Fossan, G. J. Lane, and I. Ragnarsson, Phys. Rep. **322**, 1 (1999).
[31] T. Bengtsson, Nucl. Phys. A **512**, 124 (1990).
[32] B. G. Carlsson, I. Ragnarsson, R. Bengtsson, E. O. Lieder, R. M. Lieder, and A. A. Pasternak, Phys. Rev. C **78**, 034316 (2008).
[33] H.-L. Ma, B. G. Carlsson, I. Ragnarsson, and H. Ryde, Phys. Rev. C **90**, 014316 (2014).
[34] X. Wang, M. Riley, J. Simpson, E. Paul, J. Ollier, R. Janssens, A. Ayangeakaa, H. Boston, M. Carpenter, C. Chiara, U. Garg, D. Hartley, D. Judson, F. Kondev, T. Lauritsen, N. Lumley, J. Matta, P. Nolan, M. Petri, J. Revill, L. Riedinger, S. Rigby, C. Unsworth, S. Zhu, and I. Ragnarsson, Phys. Lett. B **702**, 127 (2011).
[35] C. J. Chiara, D. G. Sarantites, M. Montero, J. O'Brien, W. Reviol, O. L. Pechenaya, R. M. Clark, P. Fallon, A. Görgen, A. O. Macchiavelli, D. Ward, Y. R. Shimizu, and W. Satuła, Phys. Rev. C **73**, 021301(R) (2006).
[36] J. J. Valiente-Dobón, T. Steinhardt, C. E. Svensson, A. V. Afanasjev, I. Ragnarsson, C. Andreoiu, R. A. E. Austin, M. P. Carpenter, D. Dashdorj, G. de Angelis, F. Dönau, J. Eberth, E. Farnea, S. J. Freeman, A. Gadea, P. E. Garrett, A. Görgen, G. F. Grinyer, B. Hyland, D. Jenkins, F. Johnston-Theasby, P. Joshi, A. Jungclaus, K. P. Lieb, A. O. Macchiavelli, E. F. Moore, G. Mukherjee, D. R. Napoli, A. A. Phillips, C. Plettner, W. Reviol, D. Sarantites, H. Schnare, M. A. Schumaker, R. Schwengner, D. Seweryniak, M. B. Smith, I. Stefanescu, O. Thelen, and R. Wadsworth, Phys. Rev. Lett. **95**, 232501 (2005).